Icarus 321 (2019) 960–973

Contents lists available at ScienceDirect

Icarus

journal homepage: www.elsevier.com/locate/icarus

A laboratory-based dielectric model for the radar sounding of the martian subsurface

Yann Brouet[*,a], Patricio Becerra[a], Pierre Sabouroux[b], Antoine Pommerol[a], Nicolas Thomas[a]

[a] Physics Institute, University of Bern, Sidlerstrasse 5, CH-3012 Bern, Switzerland
[b] Institut Fresnel, Centrale Marseille, CNRS, Aix-marseille Université, UMR 7249, Campus universitaire de Saint-Jérôme, Avenue Escadrille-Normandie-Niemen, Marseille F-13013, France

ARTICLE INFO

Keywords:
Mars
Interior — Mars
Polar caps — Radar observations

ABSTRACT

For the last decade, the SHARAD radar on board NASA's Mars Reconnaissance Orbiter, and the MARSIS radar on board ESA's Mars Express, have sounded the surface and subsurface of Mars from orbit to search for and characterise water ice reservoirs. When associated with dielectric models, the regolith composition (in terms of dust, ice and voids) of the surface and subsurface can be extracted from these data. These models describe the electromagnetic properties of the material as a function of its chemical and physical properties. With the goal of improving the currently available dielectric models for Martian icy regolith, we conducted laboratory measurements of the dielectric properties of the JSC Mars-1 Martian soil simulant mixed with water ice, varying the water ice mass fraction from 0 to 76%. Our measurements were performed between 50 MHz and 2 GHz, at ambient temperature, and at 243 K. The samples had porosities between 40% and 72%. Based on these, we propose a model that relates the dielectric constant of the sounded material to its volume fraction of water ice and/or of JSC Mars-1, its porosity, and its temperature. Tuned to the relevant frequencies, our dielectric model can be used to estimate the volume fraction of water ice from the radar sounding data of SHARAD and MARSIS. It is similarly relevant for the interpretation of data from the WISDOM radar, which will be part of the science payload of the ExoMars 2020 rover.

1. Introduction

The geomorphology of the Martian surface displays extensive evidence of the episodic presence of liquid water in the past. For most of its geologically recent history however, water on Mars has been confined to deposits of ice on different regions of the planet, the locations of which vary according to cyclic changes of Mars' orbital parameters (Laskar et al., 2004). Although at present, the majority of this ice is found in massive polar deposits (Byrne, 2009), large volumes of water ice have recently been interpreted to exist in the subsurface of mid-latitude regions in the northern (Bramson et al., 2015; Bramson et al., 2017; Stuurman et al., 2016) and southern (Dundas et al., 2018) hemispheres. These lower-latitude buried ice sheets could hold the key to understanding the history of Martian climate change, including when and under which conditions liquid water was present on the surface, and even whether or not the environment was ever suitable for life. In addition, such easily accessible ice would be a primary candidate for in-situ resource utilization (ISRU) in future manned missions (Heldmann et al., 2014). The precise study of the properties of these materials and the conditions under which they exist is therefore of the utmost importance to Mars and Planetary Science.

The last decade of Mars exploration has in part been marked by the discovery and characterization of icy deposits at and below the surface by microwave radar sounders that are able to remotely probe the subsurface of the planet. The two instruments responsible for these discoveries are the Shallow Radar (SHARAD) (Seu et al., 2004) on board NASA's Mars Reconnaissance Orbiter (Zurek and Smrekar, 2007) and the Mars Advanced Radar for Subsurface and Ionosphere Sounding (MARSIS) (Jordan et al., 2009) on board ESA's Mars Express spacecraft (Schmidt, 2003). The SHARAD instrument transmits radio waves at a centre-band frequency of 20 MHz, which allow it to detect geological boundaries up to a few kilometers in depth with a vertical resolution of about 10 m (Seu et al., 2004). MARSIS transmits radio waves at lower frequencies, in the 1.8–5.0 MHz range, and thus can be sensitive to deeper geological boundaries for the same targeted area, but its vertical resolution is about one order of magnitude lower. One of the principal goals of these instruments is to assess the volume fraction of water ice in the Martian subsurface. These radar sounders measure the delay in the

* Corresponding author.
E-mail address: yann.brouet@space.unibe.ch (Y. Brouet).

https://doi.org/10.1016/j.icarus.2018.12.029
Received 6 July 2018; Received in revised form 12 December 2018; Accepted 12 December 2018
Available online 25 December 2018

time it takes the reflected portion of an emitted radio wave to return to the instrument after it has interacted with the surface and subsurface interfaces of a planetary body, as well as the attenuation of the amplitude of this radar echo. The delay time and the amplitude attenuation vary depending on the material with which the signal interacts. The electromagnetic properties of the material (represented by the relative complex permittivity and permeability) affect the physical parameters that describe the propagation of the radio waves, such as the phase velocity, the depth to which transmitted radio waves can penetrate and the coefficients of reflection and transmission of surface and subsurface interfaces. Therefore, these properties can be derived by analyzing the return of the radar signal.

In order to interpret the retrieved electromagnetic properties in terms of the physical properties and composition of the sounded materials, it is necessary to constrain in the laboratory the interaction of radar waves with materials that have a composition analogous to that of the Martian soil. Heggy et al. (2001) measured the microwave response, at the MARSIS operating frequency band, of Martian soil analogues such as pure powdered hematite and magnetite, a Djiboutian powdered basalt, and mixtures of these three components. They showed that both the real part and the imaginary part of the permittivity increase with the iron oxide content of the sample and with decreasing frequency around 1 MHz. Leuschen (1999) and Williams and Greeley (2004) performed measurements at ambient temperature on the JSC Mars-1 Martian soil simulant (hereafter JSC Mars-1; described in the next section) in the 10–1000 GHz range and in the 200–1300 MHz range, respectively. Their measurements suggest a slight decrease with frequency of the real part of the permittivity. However, Leuschen (1999) and Williams and Greeley (2004) did not report any measurements of sample bulk density, which make the comparison with other studies difficult.

These studies are relevant to the interpretation of observations of ice-free media. However, studies reporting laboratory measurements of water ice mixed with refractory Martian soil simulants are more scarce. One such study (Mattei et al., 2014) performed dielectric measurements between 20 Hz and 1 MHz on mixtures of water ice and basaltic sand collected at Mt. Etna (Italy) as an analog for the refractory material in the Martian polar deposits. These measurements allow for the extrapolation of the dielectric properties up to the SHARAD and MARSIS frequency bands, and to temperatures expected for the Martian surface and subsurface. The authors reported on measurements made on two mixtures with well-defined ice volume fractions, however, the number of mixtures measured does not allow the derivation of a dependence of the dielectric properties on ice volume fraction. Moreover, the composition of the basaltic sand was insufficiently defined in the study (e.g., its iron oxide content is not reported), and so may not be the best analogue to simulate the dielectric properties of the refractory component of the Martian surface and subsurface. The most widely cited study thus far by research seeking to relate dielectric properties to composition is that of Stillman et al. (2010), who reported permittivity measurements on mixtures of saline (calcium chloride salt) water ice and sand performed between 1 mHz and 1 MHz. As the ice volume fraction dependence of the real part of the permittivity of the measured mixtures is well constrained, the dielectric model derived from these measurements currently represents the only dielectric mixing model used to assess the water ice volume fraction in the Martian subsurface (Bramson et al., 2015; Stuurman et al., 2016; Nerozzi and Holt, 2018; Ojha and Lewis, 2018, see Section 4). However, the sand used for the measurements consists of 99% pure silica, and may also not be the most appropriate material to consider when simulating the dielectric properties of the refractory component of the Martian soil, which is known to have an iron oxide content in the range of 15 wt% to 20 wt% (see e.g., Allen et al., 1998; Pettinelli et al., 2005, and references therein).

Thus, there is at present a lack of laboratory measurements dedicated to the characterization of the dielectric properties of icy Martian analogue materials that would be relevant for the interpretation of the SHARAD and MARSIS data. In addition, the Water Ice Subsurface Deposit Observation on Mars (WISDOM) is a ground penetrating radar that will be part of the science payload of the ExoMars 2020 Rover (Ciarletti et al., 2017), and will add measurements between 500 MHz and 3 GHz to the growing Martian microwave dataset. Therefore, dedicated laboratory measurements relevant to all three instruments is increasingly important. This paper provides new dielectric constraints on mixtures consisting of JSC Mars-1 and pure water ice based on laboratory measurements in the radar frequency range. Although we acknowledge that JSC Mars-1 is only a simulant and is not necessarily representative of the whole Martian surface and subsurface, we believe that analysing mixtures of ice with a material that simulates some of the metallic composition of the Martian soil, such as JSC Mars-1, is a significant improvement over past studies. We therefore propose new dielectric models at frequencies relevant for MARSIS, SHARAD and WISDOM, which allow estimates of the ice volume fraction of the Martian subsurface in the sounded regions.

2. Methods

2.1. Samples

We used the facilities developed in the LOSSy laboratory at the University of Bern to produce pure and quasi-spherical water ice particles with a type Ih crystalline structure (Bartels-Rausch et al., 2012). A cryogenic scanning electron microscope analysis of these water ice particles shows a mean particle diameter equal to 67 ± 31 μm (e.g., Yoldi et al., 2015). The technique used for the preparation of the water ice samples with this mean particle diameter is extensively described in Yoldi et al. (2015), Poch et al. (2016) and Brouet et al. (2016).

JSC Mars-1 consists of volcanic ash collected on the Pu'u Nene volcanic cone, located on the southern flank of Mauna Kea in Hawai'i (Allen et al., 1998). The iron oxide content of the volatile-free JSC Mars-1 is relatively close to the values of 15.6 wt% measured by the Viking and Pathfinder landers (see Table 1 in Allen et al., 1998). The procedure developed in the LOSSy laboratory to prepare homogeneous

Table 1
Physical characteristics of the JSC Mars-1 samples and the mixtures, consisting of water ice and JSC Mars-1, prepared for the dielectric measurements. F_D is the dust mass fraction of the mixtures; ρ, the bulk density and σ_ρ its uncertainty; Φ_a, the porosity and σ_{Φ_a} its uncertainty. The uncertainties were calculated through error propagation. The samples #1–4 and #5–23 were measured at temperatures of 298 K and 243 K, respectively.

Sample #	F_D	ρ ± $\sigma\rho$ (kg.m^{-3})	Φ_a ± σ_{Φ_a} (%)
1	1.00	715 ± 18	71.1 ± 0.7
2		841 ± 20	66.0 ± 0.8
3		858 ± 21	65.4 ± 0.8
4		878 ± 21	64.5 ± 0.9
5	1.00	804 ± 20	67.5 ± 0.8
6		830 ± 20	66.5 ± 0.8
7		841 ± 20	66.0 ± 0.8
8		858 ± 21	65.4 ± 0.8
9		878 ± 21	64.5 ± 0.9
10	0.70	691 ± 17	57.9 ± 1.1
11		701 ± 17	57.2 ± 1.1
12		729 ± 18	55.5 ± 1.2
13		790 ± 19	51.8 ± 1.2
14		801 ± 19	51.1 ± 1.3
15	0.49	581 ± 15	56.2 ± 1.1
16		656 ± 17	50.6 ± 1.3
17		713 ± 18	46.3 ± 1.3
18		742 ± 18	44.1 ± 1.4
19	0.24	439 ± 12	59.2 ± 1.2
20		552 ± 15	48.7 ± 1.4
21		564 ± 15	47.6 ± 1.4
22		636 ± 16	40.9 ± 1.5
23		637 ± 16	40.8 ± 1.5

Table 2
Parameters used in the Cole–Cole relaxation model to fit the data as a function of frequency for samples #1–#18. E_a is the activation energy, α is the Cole–Cole distribution parameter, τ_∞ is the time constant of relaxation at infinite temperature, ϵ'_{DC} and ϵ'_∞ are the low and high frequency limits of ϵ', respectively.

	Cole–Cole model parameters				
Sample #	$E_a(eV)$	α	τ_∞ (ns)	ϵ'_{DC}	ϵ'_∞
1	1.7e−01 ± 3.4e−06	5.7e−03 ± 1.5e−02	6.0e−05 ± 1.4e−06	2.3e+00 ± 2.8e−03	1.60
2	1.7e−01 ± 2.2e−06	1.2e−01 ± 1.4e−02	5.5e−05 ± 1.4e−06	2.8e+00 ± 4.2e−03	1.74
3	1.6e−01 ± 1.2e−06	3.7e−01 ± 1.7e−02	4.5e−05 ± 1.5e−06	3.1e+00 ± 8.4e−03	1.76
4	1.6e−01 ± 1.2e−06	4.3e−01 ± 1.9e−02	4.5e−05 ± 1.5e−06	3.1e+00 ± 1.2e−02	1.78
5	1.6e−01 ± 8.4e−07	6.9e−01 ± 2.3e−02	3.7e−05 ± 1.1e−05	2.7e+00 ± 4.9e−02	1.70
6	1.6e−01 ± 7.5e−07	6.1e−01 ± 1.1e−02	3.8e−05 ± 2.9e−06	2.9e+00 ± 2.1e−02	1.73
7	2.4e−01 ± 4.4e−04	8.2e−01 ± 3.1e−02	1.5e−03 ± 7.6e−03	4.5e+00 ± 1.5e+00	1.74
8	1.6e−01 ± 1.2e−06	6.1e−01 ± 1.6e−02	4.2e−05 ± 5.5e−06	3.0e+00 ± 3.6e−02	1.76
9	1.7e−01 ± 1.1e−06	6.7e−01 ± 1.7e−02	5.9e−05 ± 1.6e−05	3.3e+00 ± 6.9e−02	1.78
10	1.6e−01 ± 6.9e−07	6.8e−01 ± 1.5e−02	4.2e−05 ± 8.1e−06	2.7e+00 ± 3.9e−02	1.56
11	1.6e−01 ± 4.5e−07	6.0e−01 ± 7.8e−03	2.9e−05 ± 1.1e−06	2.7e+00 ± 1.1e−02	1.59
12	1.6e−01 ± 1.1e−06	5.5e−01 ± 1.2e−02	3.7e−05 ± 2.1e−06	2.7e+00 ± 1.8e−02	1.61
13	1.6e−01 ± 2.5e−06	2.8e−01 ± 1.8e−02	1.4e−05 ± 5.2e−07	2.9e+00 ± 6.8e−03	1.68
14	1.6e−01 ± 7.0e−07	6.0e−01 ± 9.7e−03	3.0e−05 ± 1.5e−06	3.0e+00 ± 1.7e−02	1.69
15	1.5e−01 ± 1.0e−06	3.9e−01 ± 1.0e−02	1.8e−05 ± 3.0e−07	2.1e+00 ± 2.9e−03	1.47
16	1.5e−01 ± 7.0e−07	6.5e−01 ± 2.5e−02	1.2e−05 ± 5.9e−07	2.6e+00 ± 2.5e−02	1.54
17	9.4e−02 ± 1.4e−06	4.5e−02 ± 1.2e−02	4.4e−04 ± 1.0e−05	2.6e+00 ± 2.9e−03	1.60
18	1.5e−01 ± 8.4e−07	4.8e−01 ± 1.1e−02	2.0e−05 ± 2.9e−07	2.7e+00 ± 7.1e−03	1.63

and porous mixtures with different dust mass fractions requires a similar grain size distribution (Yoldi et al., 2015; Brouet et al., 2016). Therefore, we sieved a sample of JSC Mars-1 to constrain the mean grain size to be lower than 100 μm.

The only measurement of the mean particle density of JSC Mars-1 currently available in the literature is reported in Allen et al. (1998) and is 1.91 ± 0.02 g.cm^{-3}. This value was determined by pouring known masses of JSC Mars-1 into water and measuring the water displacement. We updated this measurement with a more accurate technique that consists of using a calibrated helium pycnometer (Upyc-1200e-V5.04). Our measurement resulted in a value of 2.52 ± 0.03 g.cm^{-3} before sieving and 2.48 ± 0.03 g.cm^{-3} after sieving. This means that the mean particle density of the sample does not depend on the grain size distribution, and that these measurements also suggest that the composition of the JSC Mars-1 sample is unaffected by this preparation procedure. We validated the technique by measuring the mean particle density of pure silica particles (= 2.63 ± 0.03 g.cm^{-3}) before measuring that of the JSC Mars-1 sample. These mean particle density measurements can then be used to calculate the porosity of the pure samples, equal to (1 - ρ/ρ$_s$), where ρ is the bulk density and ρ$_s$ is the mean particle density. We use our measurement of mean particle density after sieving in the calculation of porosities reported here.

The water content of the Martian regolith is expected to be in the range of about 3 wt% to 13 wt% (Audouard et al., 2014). The JSC Mars-1 sample was baked in an oven for 24 h at 393 K in order to reduce its residual water content (Stillman and Olhoeft, 2008), which could increase the real and imaginary parts of the permittivity (see e.g., Sabouroux and Ba, 2011). This process was completed using a moisture analyzer that also provides an estimate of the volumetric water content of the sample. It was found to be less than 5%, which is within the range of water content expected for the Martian regolith (Audouard et al., 2014). After this step, and having performed the dielectric measurements at ambient temperatures as described in Section 2.2, the samples were stored in a chest freezer with a constant temperature of 243 K, which provides a relatively dry environment and cools down the dust sample.

In addition to the pure JSC Mars-1 and water ice samples, we prepared mixtures of the two components with dust mass fractions equal to 0.24, 0.49 and 0.70. We used the same well-defined mixing procedure described in Yoldi et al. (2015), Poch et al. (2016) and Brouet et al. (2016), the latter of which also report dielectric measurements between 50 MHz and 2 GHz of pure water ice samples, pure JSC-1A Lunar simulant, and mixtures of the two. The porosity of the water ice-dust mixture is $\Phi_a = 1 - \rho \times (F_D/\rho_D + (1 - F_D)/\rho_I)$, where F_D, is the dust mass fraction of the sample, ρ_D the mean particle density of the dust, and ρ_I the mean particle density of the water ice, equal to 0.917 g.cm^{-3} for type Ih crystalline water ice (Lide, 2005). The values of porosity vary between 64% for compacted and 72% for non-compacted samples of pure JSC Mars-1, and the porosity of the mixtures varies between 40% and 60%. The physical properties of all samples in this study are presented in Table 1.

2.2. Laboratory setup

All measurements of the complex permittivity were performed at the Laboratory for Analysis of Planetary and Interplanetary Data Sets (LAPIS) of the University of Bern (Switzerland) in August 2017. The measurements of the pure JSC Mars-1 samples were performed at ambient temperature and at 243 K, and those involving the water ice and the icy mixtures were performed only at 243 K. All measurements were completed under ambient pressure.

We repeated the measurement procedure developed for porous, icy and silicate-rich media in the range of 50 MHz to 2 GHz described in detail in Brouet et al. (2016). This procedure consists of measuring the scattering parameters of each of the two ports of a coaxial cell connected to a vector network analyser (Anritsu Master MS2038C). The procedure includes a full SOLT (Short-Open-Load-Through) calibration step performed before each series of measurements with a given sample holder with a filled volume of 1.291 ± 0.288 cm^3, at the reference planes of the connectors of the coaxial cell. For all samples, the scattering parameters are measured over 201 frequencies between 50 MHz and 2 GHz. A Nicolson-Ross procedure is applied to determine the real and the imaginary parts of the permittivity at a given frequency from each pair of scattering parameters (Nicolson and Ross, 1970). The mean of the two values of the real part and that of the two values of the imaginary part of the permittivity are taken to be the real and imaginary parts of the permittivity of a sample at a given frequency. For more details about the coaxial cell and the acquisition method, see Georget et al. (2014) and Brouet et al. (2016).

3. Results

Figs. 1–5 shows the means of the real and imaginary parts of the permittivity, ϵ' and ϵ'', taking into account the scattering parameters

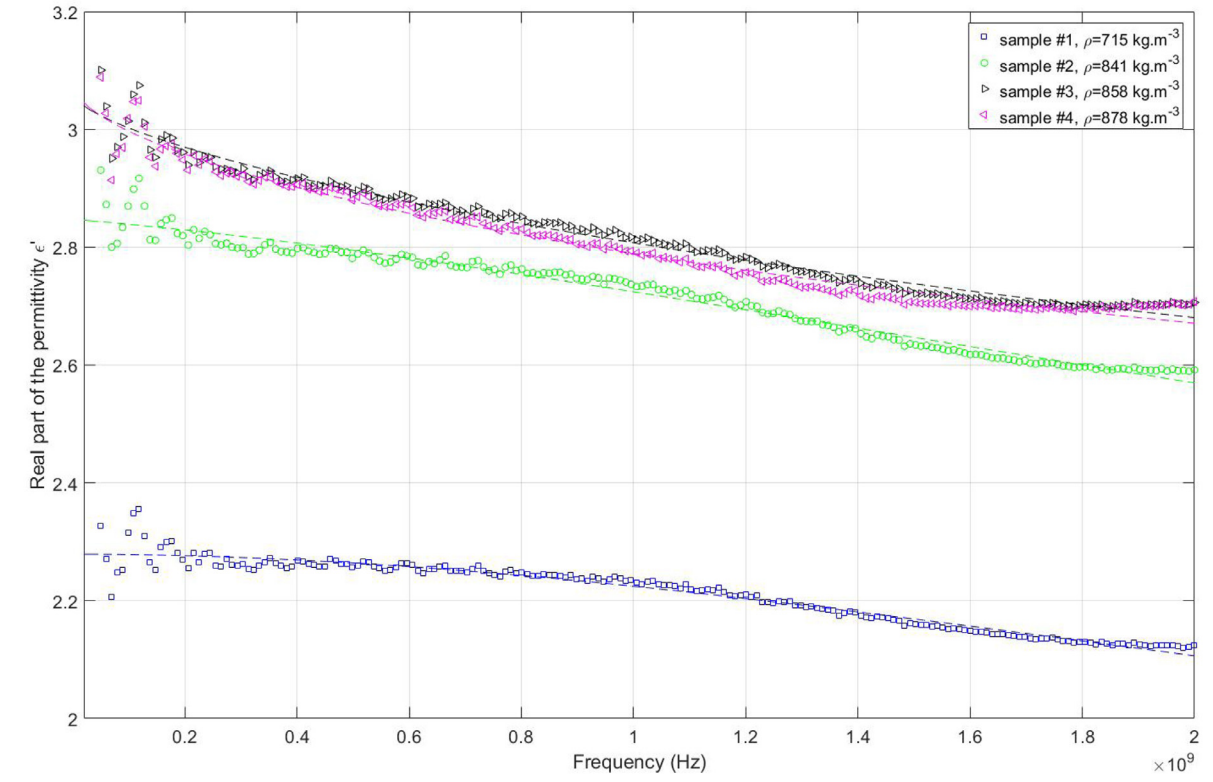

(a)

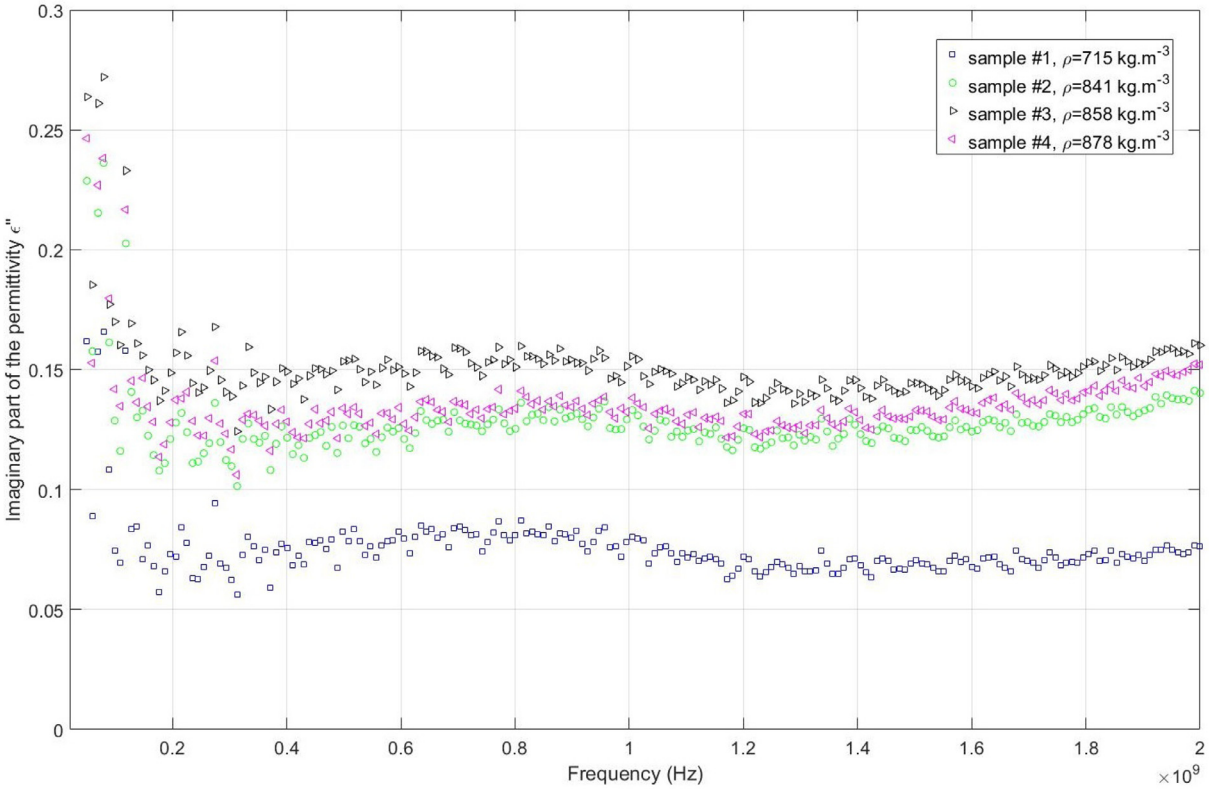

(b)

Fig. 1. Real part (a), ϵ', and imaginary part (b), ϵ'', of the complex permittivity as a function of frequency between 50 MHz and 2 GHz for samples #1, #2, #3 and #4 at 298 K. Dashed lines represent the values of ϵ' obtained from a Cole–Cole model fit to the data extrapolated to 20 MHz.

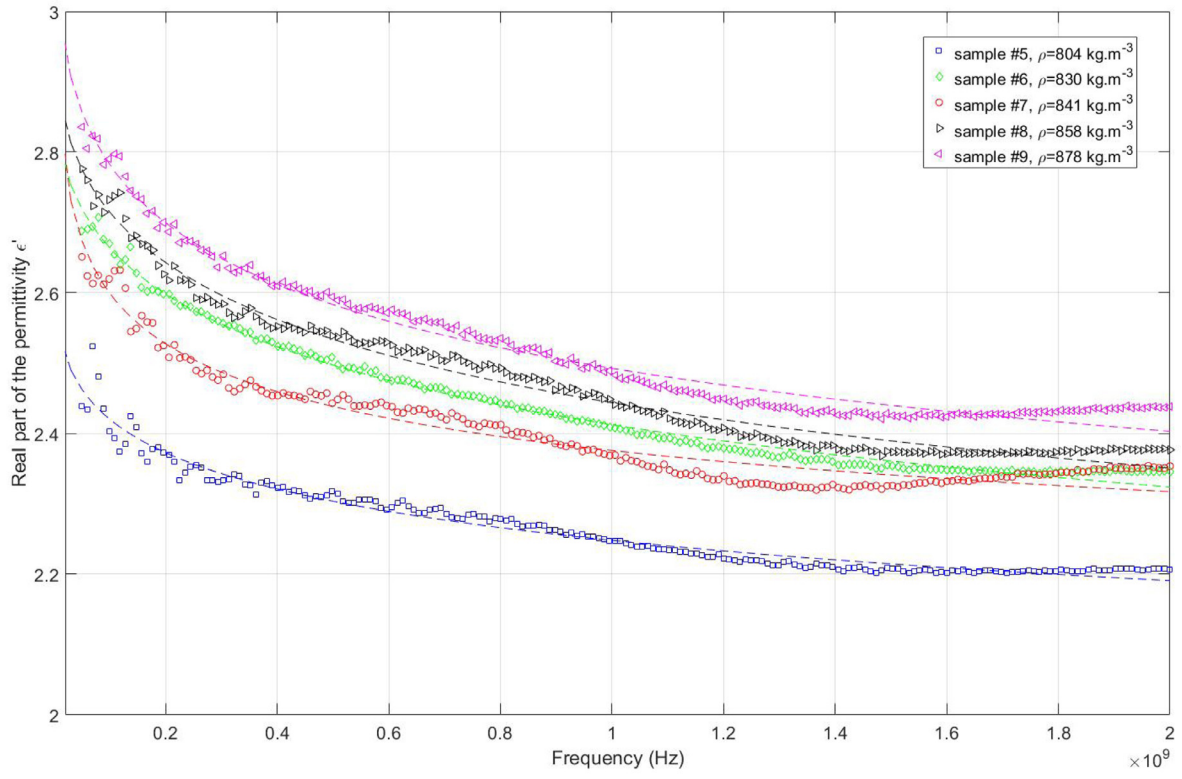

(a)

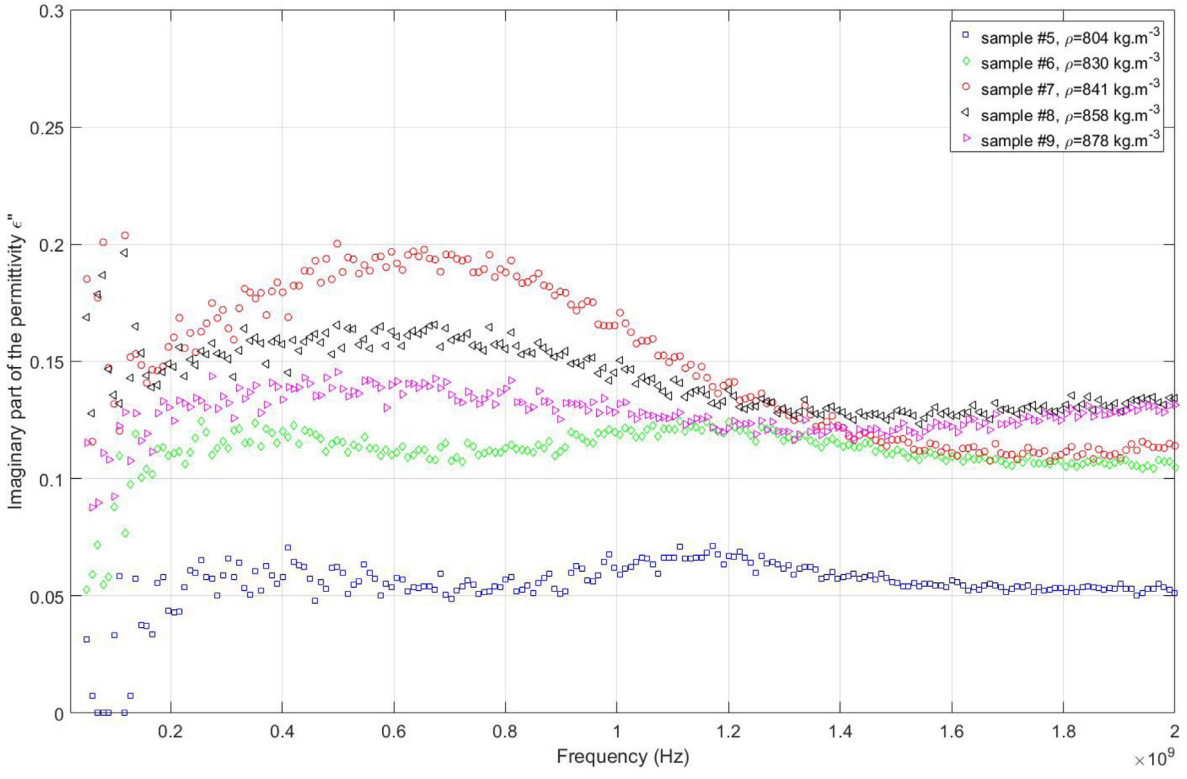

(b)

Fig. 2. Real part (a), ϵ', and imaginary part (b), ϵ'', of the complex permittivity as a function of frequency between 50 MHz and 2 GHz for samples #5, #6, #7, #8 and #9 at 243 K. Dashed lines represent the values of ϵ' obtained from a Cole–Cole model fit to the data, extrapolated to 20 MHz.

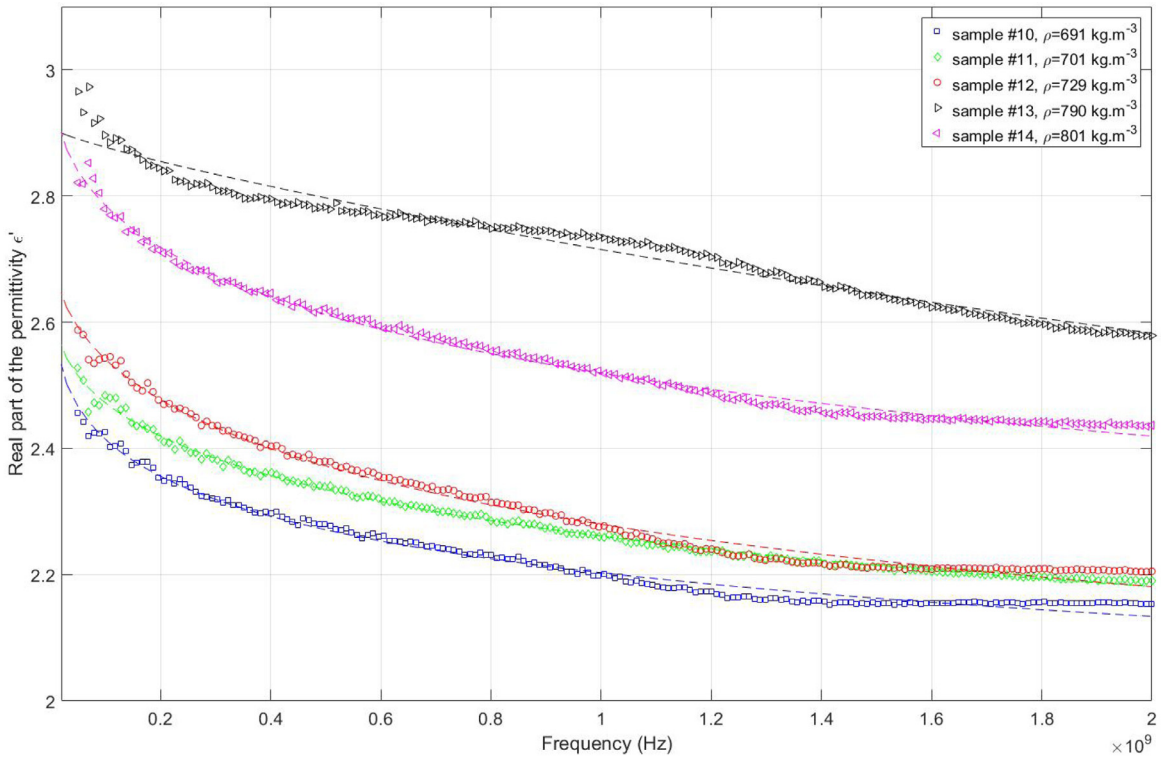

(a)

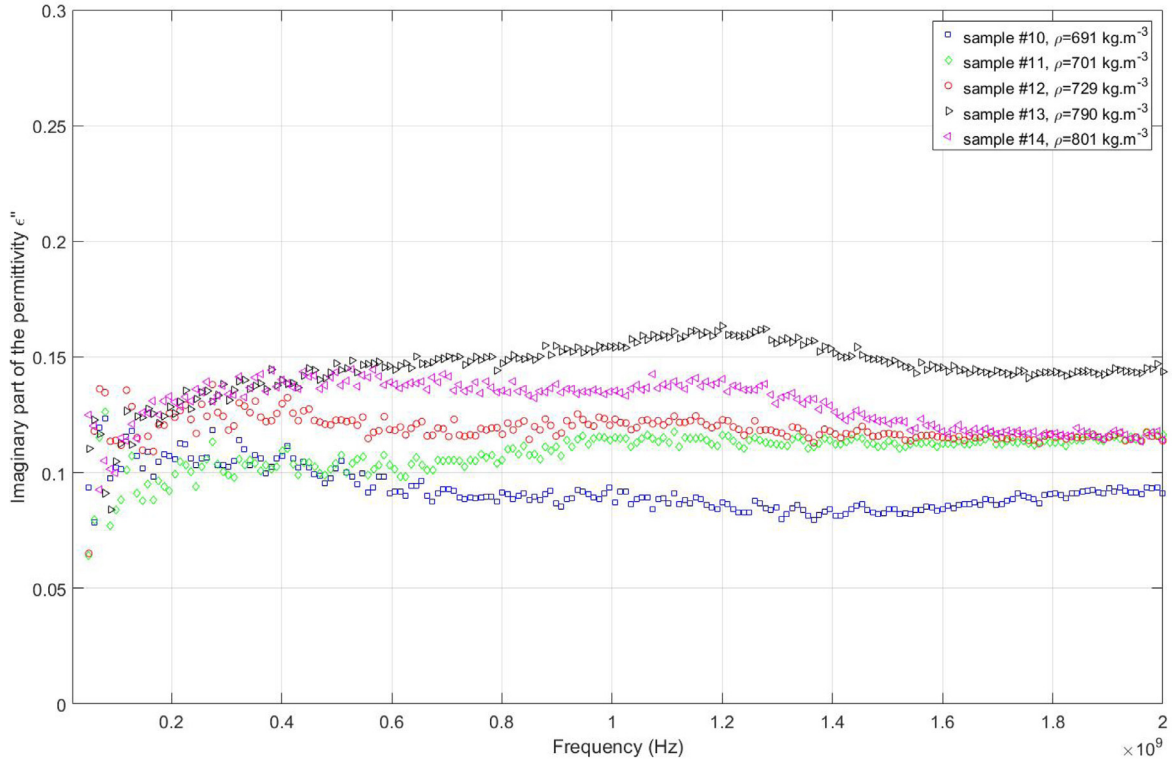

(b)

Fig. 3. Real part (a), ϵ', and imaginary part (b), ϵ'', of the complex permittivity as a function of frequency between 50 MHz and 2 GHz for samples #10, #11, #12, #13 and #14 at 243 K. Dashed lines represent the values of ϵ' obtained from a Cole–Cole model fit to the data, extrapolated to 20 MHz.

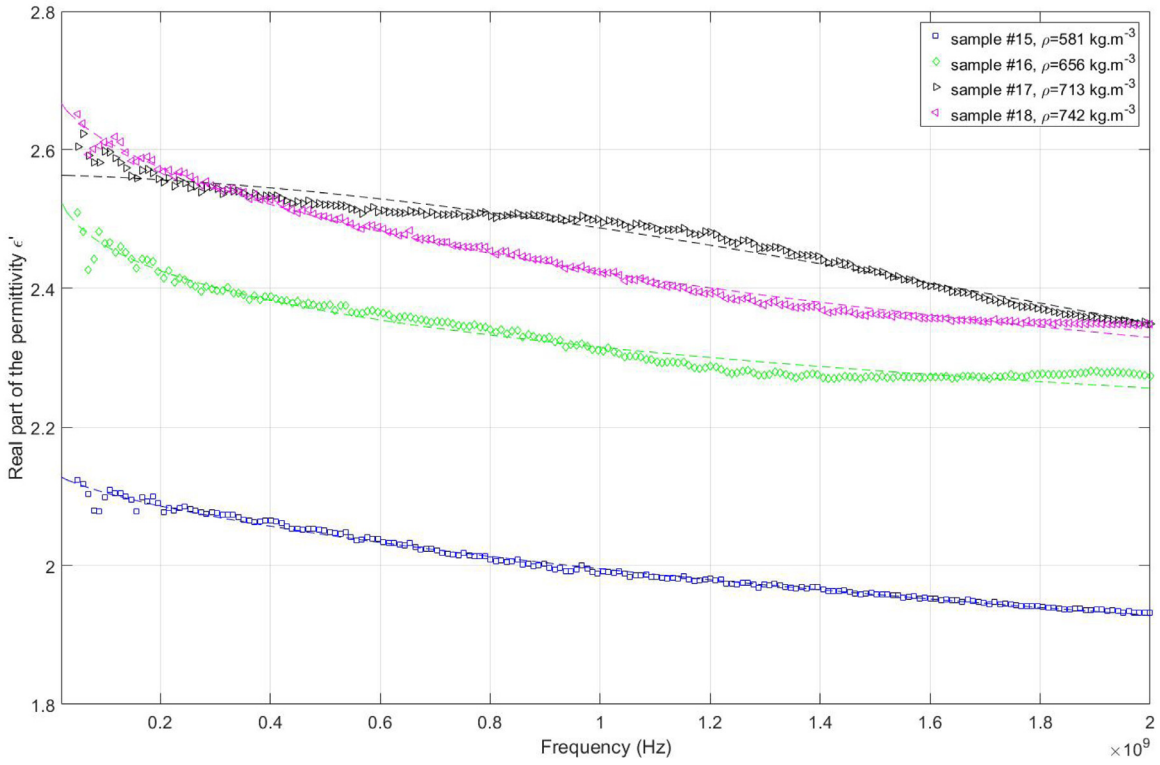

(a)

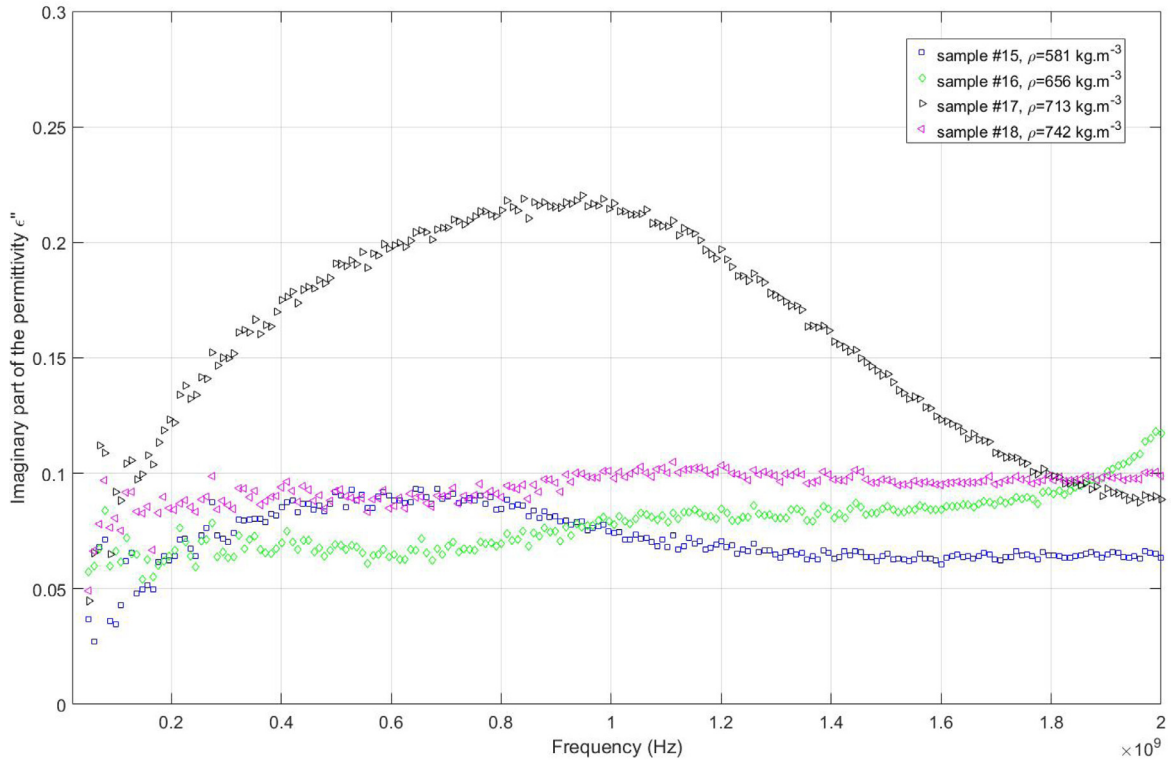

(b)

Fig. 4. Real part (a), ϵ', and imaginary part (b), ϵ'', of the complex permittivity as a function of frequency between 50 MHz and 2 GHz for samples #15, #16, #17 and #18 at 243 K. Dashed lines represent the values of ϵ' obtained from a Cole–Cole model fit to the data, extrapolated to 20 MHz.

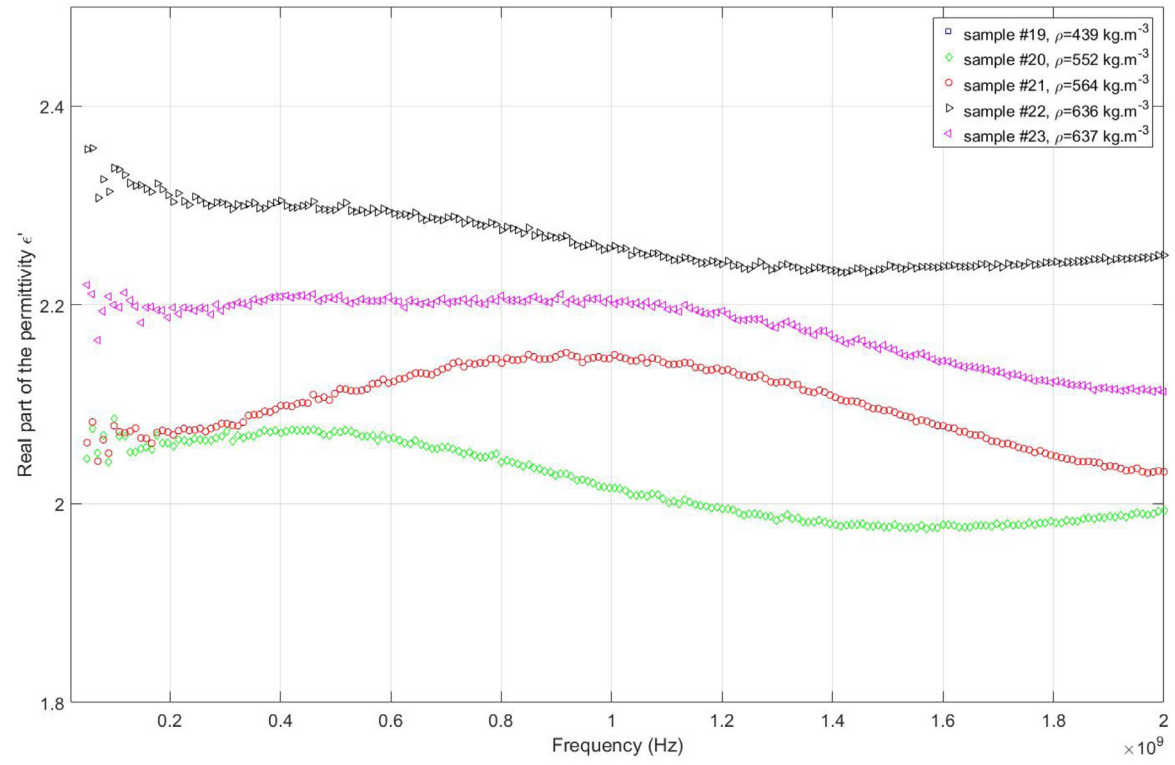

(a)

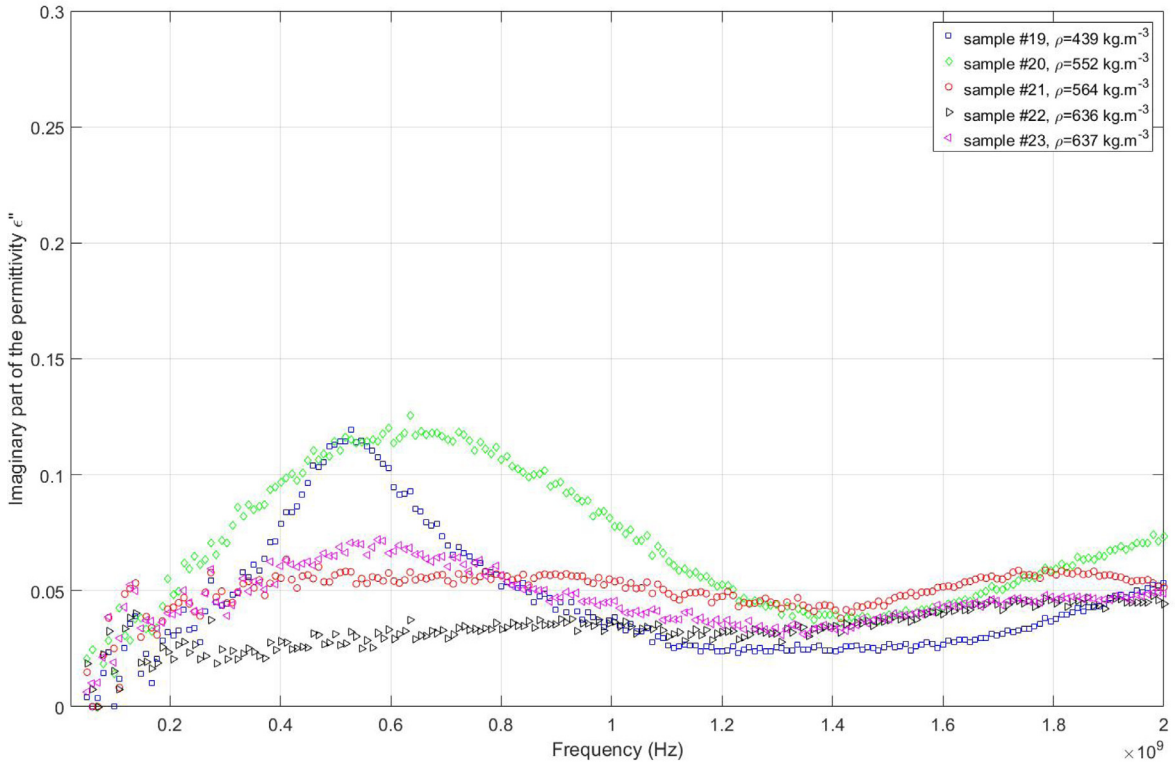

(b)

Fig. 5. Real part (a), ϵ', and imaginary part (b), ϵ'', of the complex permittivity as a function of frequency between 50 MHz and 2 GHz for samples #19, #20, #21, #22 and #23 at 243 K. Dashed lines represent the values of ϵ' obtained from a Cole–Cole model fit to the data, extrapolated to 20 MHz.

measured at the two coaxial ports of samples #1–#4, #5–#9, #10–#14, #15–#18 and #19–#23, respectively, as a function of the frequency. The absolute experimental uncertainty is evaluated to be equal or lower than 10% (Brouet et al., 2016; Georget et al., 2014). Using all measured samples and the range of frequencies noted in the previous section, ϵ' varies between 1.6 and 3.0. For samples with a dust mass fraction greater or equal to 49% (#1–#18), we notice a slight decrease of ϵ' with the frequency. This decrease is larger than the uncertainty of the measurements but remains lower than 17% from 50 MHz to 2 GHz. This trend was also observed with the original non-sieved JSC Mars-1 sample by Leuschen (1999), Williams and Greeley (2004) and Stillman and Olhoeft (2008) over similar frequency ranges at a temperature of $\sim$ 298 K. It has been interpreted as a slight dielectric relaxation potentially caused by an interfacial polarization created by residual adsorbed water (Stillman and Olhoeft, 2008) that survives the drying step involved in the preparation of each sample. Stillman and Olhoeft (2008) note that, in the context of subsurface radar sounding of Mars, adsorbed water must be taken into account when assessing the penetration depth of the radar waves, so this effect (only measurable in samples with a dust mass fraction equal to or larger than 49%) is a realistic one that should be considered, and therefore does not diminish the reliability of our results.

Results for samples #2, #3 and #4 at ambient temperature, and samples #7, #8 and #9 at 243 K, enable us to estimate the temperature dependence of ϵ' for the pure JSC Mars-1 sample. The permittivity of silicate-rich material has been experimentally determined to increase linearly with temperature (Campbell and Ulrichs, 1969; Calla and Rathore, 2012). We estimate that the slope of this linear dependence is of the order of 10^{-3}, similarly to water ice for the same frequency range (e.g., Ulaby and Long, 2014). Our results are also consistent with previous experimental studies of basaltic samples (Campbell and Ulrichs, 1969; Heggy et al., 2001; Brouet et al., 2016) and with predictions from dielectric mixing laws (Sihvola, 1999; Ulaby and Long, 2014), which show an increase of ϵ' with the bulk density.

Because of the relatively high volume fraction of air, all samples show a low magnitude of dielectric loss, expressed by the imaginary part of the permittivity being lower than 0.3. In addition to the high content of air in the samples, the presence of water ice in the mixtures further lowers the dielectric losses, as ϵ'' for solid water ice is lower than the value expected for a solid silicate-rich or basaltic material in the relevant frequency range (Campbell and Ulrichs, 1969; Mattei et al., 2014). ϵ'' varies slightly with frequency, but this variation is considered negligible because it remains below the uncertainty of the measurement of ϵ'', which is estimated to be ≤ 0.1 by propagating the uncertainties of the experimental and scattering parameters (Georget et al., 2014). The mean of ϵ'' calculated over the measured frequency range, ϵ''_m, has been taken into account to infer the porosity dependence. Fig. 6 shows that for samples with dust mass fractions equal to 0.49, 0.70 and 1, an overall decrease of ϵ''_m with porosity increases exists, which is in agreement with other experimental and theoretical results (Sihvola, 1999; Ulaby and Long, 2014). In the samples with a dust mass fraction of 0.24, no porosity dependence was measured, as the sensitivity limit of the instrument to the dielectric losses is reached for ϵ'' lower than 0.1. Also, the results do not show a clear temperature dependence for pure JSC Mars-1 measurements performed at 298 K and 243 K. This sensitivity limit prevents any further analysis of the measured ϵ''. However, this does not affect the direct implications of this study, which are based on analyses of ϵ' only, since our study - and most SHARAD/MARSIS data analysis to date - assumes the specific case of radar sounding through low-loss materials.

The real and imaginary parts of the complex magnetic permeability of the samples were also determined. At 298 K, the results show that the JSC Mars-1 sample is nonmagnetic at radar frequencies, with a real part of the magnetic permeability below 1.1 over the measured frequency range and an imaginary part lower than 0.1. This was expected from the measurements performed by Williams and Greeley (2004) and Stillman and Olhoeft (2008).

4. Implications for radar-based investigations of the martian subsurface

A remote subsurface sounding radar can detect dielectric interfaces in the subsurface due to the echo caused by the interaction of the transmitted radio waves with media of varying dielectric properties. Information on the local topography can help differentiate real subsurface returns from those caused by sloping, off-nadir surfaces (known as “clutter”; Holt et al., 2006). In addition, detailed topographic measurements can constrain the depth of a reflection interface identified by the radar (Bramson et al., 2015). The combination of topographic data with radargrams (along-track images of radar return power versus delay time) allows a link to be made between the delay time associated with a given reflector and the dielectric and magnetic properties of the overlying material. For a nonmagnetic and low-loss material, one can directly convert the delay time to an effective real part of the permittivity, ϵ'. Then, ϵ' can be expressed as a function of the volume fraction and the zero-porosity value of ϵ' of each individual component by applying a dielectric mixing model (Sihvola, 1999). Using this method and assuming a Martian subsurface consisting of water ice, silicate-rich dust and air, various studies determined the volume fraction of water ice present in the subsurface at different locations in the Northern (Bramson et al., 2015; Stuurman et al., 2016; Dundas et al., 2018) and Southern (Dundas et al., 2018) hemispheres from SHARAD radargrams, and discussed the implications of these studies for the hydrologic history of Mars. These studies used the following three-phase power-law of Stillman et al. (2010) to convert the estimated dielectric constant to an estimated ice volume fraction:

$$\epsilon'^{1/\gamma} = \epsilon'^{1/\gamma}_D \times \Phi_D + \epsilon'^{1/\gamma}_I \times \Phi_I + \epsilon'^{1/\gamma}_a \times \Phi_a \quad (1)$$

Here, ϵ'_D and ϵ'_I, are the zero-porosity value of ϵ' for the dust and the ice, respectively; ϵ'_a, is ϵ' of air (= 1); Φ_D, Φ_I and Φ_a, are the volume fractions of dust, ice and air, respectively.

Stillman et al. (2010) performed laboratory measurements of the permittivity of sand-saline (calcium chloride) water ice mixtures and a constant porosity equal to 46%. These experiments were done at a temperature of 181 K and with a radar frequency of 1 Hz. Based on a best fit to their measurements, they estimated the power-law exponent γ to be 2.7 $\pm$ 0.3. The value of the power-law exponent is independent of the frequency. Instead, in theoretical dielectric mixing laws, it is a direct consequence of the geometry of the particles considered to be interacting with a homogeneous electric field (see e.g., Looyenga, 1965; Sihvola, 1999). Therefore, the value of γ used by Stillman et al. (2010) remains valid for an air-ice-sand mixture at the SHARAD operating frequency, although the shape of the particles is not constrained. However, the sand used for these measurements (U.S. Silica OK-110) consists of high-purity silica grains (larger than 99 wt%), and Martian soils were found to have an iron oxide content in the range of 15 wt% to 20 wt% (Allen et al., 1998). Thus, the dust component used in the Stillman et al. (2010) study may not be the best analogue for Martian soils, while compositionally, the JSC Mars-1 simulant can be considered a better analogue for Martian soil than sand due to its iron oxide content (Allen et al., 1998). Furthermore, the power-law exponent of Eq. (1) takes into account the effect on ϵ' of the calcium chloride salt that was dissolved in the liquid water sample used to make the ice, which is not taken into account in the studies that propose an interpretation of SHARAD radargrams based on this equation (Bramson et al., 2015; Stuurman et al., 2016; Nerozzi and Holt, 2018). We therefore propose an alternative dielectric model to invert SHARAD radargrams to target composition based on the laboratory measurements presented above.

In order to determine ϵ' values at 20 MHz for samples #1–#18, we apply the same approach reported in Stillman and Olhoeft (2008), and

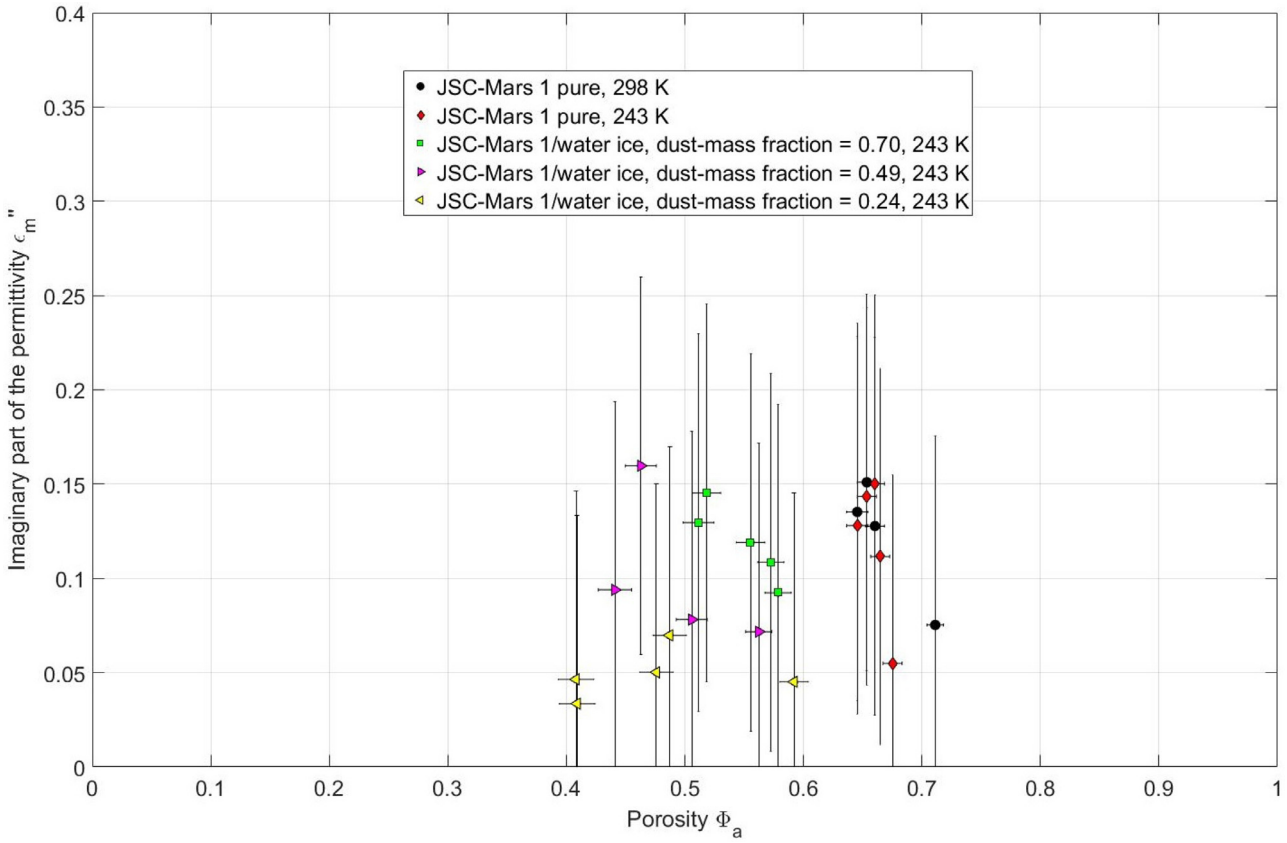

Fig. 6. Mean of the imaginary part of the permittivity (ϵ''_m) calculated over the relevant frequency range as a function of the porosity (Φ_a) for pure JSC Mars-1 samples measured at 298 K and 243 K, and for mixtures consisting of JSC Mars-1 and pure water ice with dust mass fractions equal to 0.70, 0.49 and 0.24. The error bars represent the maximum experimental uncertainty.

model the dielectric relaxation of ϵ' with the following broad Cole–Cole relaxation model (Cole and Cole, 1941):

$$\epsilon = \epsilon' - i\epsilon'' = \epsilon_\infty + \frac{\epsilon_{DC} - \epsilon_\infty}{1 + (i\omega\tau)^\alpha} \quad (2)$$

Here, the real part ϵ' can be expressed as a function of the angular frequency, ω, and the low-frequency and the high-frequency limits of ϵ', ϵ'_{DC} and ϵ'_∞. The Cole-Cole distribution parameter, α, describes the log-normal distribution of the time constants of the dielectric relaxations. For a perfectly homogeneous material, it is equal to 1, and the Cole–-Cole equation reduces to the single-relaxation Debye model (Debye, 1929). The time constant of relaxation, τ, can be predicted using the generalized Boltzmann temperature dependence:

$$\tau = \tau_\infty e^{\frac{E_a}{kT}}, \quad (3)$$

where E_a is the activation energy, k is Boltzmann's constant (8.6176×10^{-5} eV/K), and T is the temperature. The high frequency limit of ϵ' is calculated using a Lichtenecker power law mixing formula, $\epsilon'_\infty = 1.93^\rho$, as reported in Stillman and Olhoeft (2008), where ρ is the bulk density in g.cm^{-3}. For more details, one can refer to Cole and Cole (1941) and Stillman and Olhoeft (2008). The values of the Cole-Cole fit parameters are shown in Table 2. For samples #19–#23, there is no measurable dielectric relaxation of ϵ', as its maximum variation between 50 MHz and 2 GHz is lower than the measurement uncertainty. Thus, we considered the mean of the ϵ' values over the frequency range of measurement to be representative of ϵ' at 20 MHz.

Then, we used the values of the Cole–Cole parameters reported in Table 2 to determine ϵ' at SHARAD center-band operating frequency. The results are presented in Table 3. As an example, Fig. 7 shows the estimated values of the real part of the effective permittivity at the SHARAD operating frequency as a function of the porosity Φ_a.

Table 3
Real part of the effective permittivity predicted from the Cole-Cole relaxation model, ϵ'_{C-C}, at 2 MHz, 20 MHz, 500 MHz and 3 GHz for each sample. The values are calculated using the parameters in Table 2. The mean of the real part of the effective permittivity over the frequency range ϵ'_m, is determined to be representative of samples #19–23, as its maximum variation is lower than the uncertainty of the measurements.

	ϵ'_{C-C} at a frequency equal to			
Sample #	2 MHz	20 MHz	500 MHz	3 GHz
1	2.28	2.28	2.26	1.99
2	2.85	2.85	2.79	2.43
3	3.06	2.90	2.81	2.59
4	3.07	3.04	2.88	2.59
5	2.60	2.51	2.30	2.16
6	2.87	2.78	2.50	2.27
7	3.06	2.78	2.44	2.28
8	2.94	2.84	2.53	2.30
9	3.10	2.94	2.58	2.35
10	2.63	2.53	2.27	2.09
11	2.63	2.56	2.33	2.13
12	2.71	2.64	2.37	2.12
13	2.91	2.90	2.80	2.48
14	2.98	2.90	2.61	2.36
15	2.14	2.13	2.04	1.88
16	2.57	2.52	2.37	2.22
17	2.56	2.56	2.54	2.21
18	2.69	2.67	2.50	2.27
	ϵ'_{mean} [0.05–2 GHz]			
19	1.69			
20	2.02			
21	2.01			
22	2.27			
23	2.18			

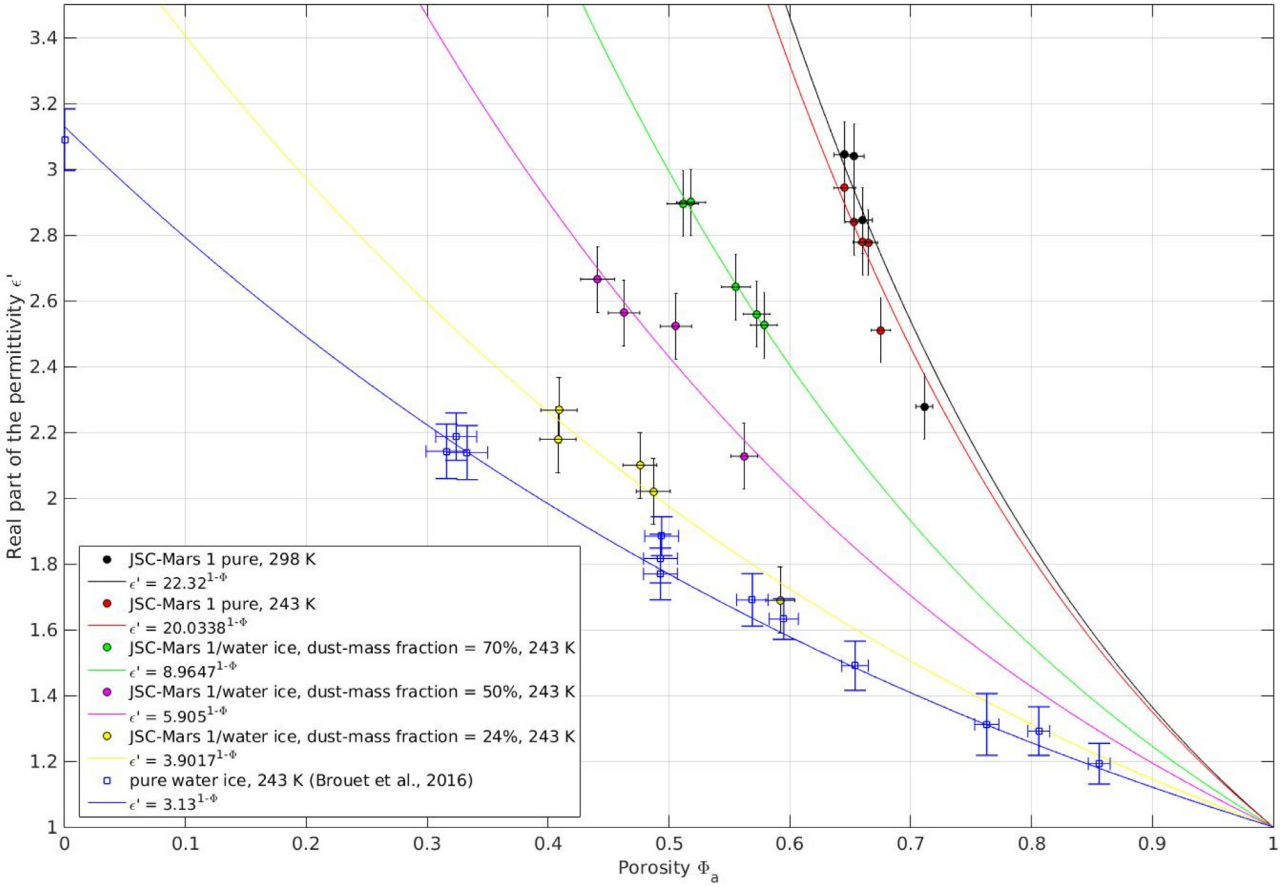

Fig. 7. Real part of the permittivity (ϵ') as a function of the porosity (Φ_a) of pure JSC Mars-1 at 298 K and 243 K, and mixtures of JSC Mars-1 and pure water ice with dust mass fractions equal to 0.70, 0.49 and 0.24. The curves are obtained from regression analyses applied to the data with $E^{(1-\Phi_a)}$. The correlation coefficients are larger than 0.98, and the fit coefficients are estimated with 95% confidence. The error bars represent the maximum experimental uncertainty.

Based on the method reported in Brouet et al. (2016), the variation of ϵ' as a function of Φ_a for a given dust mass fraction F_D is modeled with $E^{(1-\Phi_a)}$. The E coefficient represents $(\epsilon'_D/\epsilon'_I)^{\Phi_D} \times \epsilon'_I$, with ϵ'_D and ϵ'_I, the zero-porosity values of the real part of the permittivity of dust and pure water ice, respectively, and Φ_D, the volume fraction of dust of the sample. This expression for E is derived from the Lichtenecker mixing equation, which also successfully models the bulk density dependence of ϵ' obtained from 92 measurements of Lunar soil samples (Olhoeft and Strangway, 1975). The variation of the E coefficient as a function of the dust mass fraction at a given frequency is then modeled by the following equation, as shown in Fig. 8:

$$\epsilon' = (P_1^{F_D} + P_2)^{1-\Phi_a}, \tag{4}$$

where $F_D = \frac{\rho_D \Phi_D}{\rho_D \Phi_D + \rho_I \Phi_I}$, is the dust mass fraction, and Φ_D, Φ_I and Φ_a are the volume fractions of JSC Mars-1 simulant, water ice and air in the mixture, respectively. ρ_D and ρ_I are the solid density of the JSC Mars-1 simulant and the pure crystalline water ice. Empirical parameters P_1 and P_2 are indicated in Table 4. Taking into account the temperature dependence of ϵ' of water ice and JSC Mars-1, the resulting dielectric mixing model is:

$$\epsilon' = \left(P_1^{\frac{\rho_D \Phi_D}{\rho_D \Phi_D + \rho_I \Phi_I}} + P_2 \right)^{1-\Phi_a} + (T - 243) \times 10^{-3}, \tag{5}$$

where T is the temperature.

Fig. 9 shows ϵ' of a three-phase mixture as a function of the volume fraction of air, and for different values of water ice volume fraction. This figure compares the curves obtained by the three-phase mixing law of Stillman et al. (2010) to those obtained with Eq. (5) for a temperature of 200 K (taken to be the Martian mean surface temperature at the relevant latitudes, Mellon et al., 2004), and using the upper limit of the P_2 parameter (i.e., 2.16). This makes the model consistent with the zero-porosity value of pure water ice at 20 MHz ($\epsilon'_I = 3.1 - 3.2$, see e.g., Gough, 1972; Mätzler and Wegmuller, 1987) with volume fractions of dust and air equal to 0. A maximum value of porosity equal to 50% is chosen, as it is assumed to be the upper limit of porosity associated to the Martian surface (see e.g., Bramson et al., 2015). The two dielectric models lead to different interpretations of ϵ' in terms of the composition of the Martian subsurface. For instance, for $\epsilon' = 2.5$, the maximum value of water ice volume fraction permitted by Eq. (5) is estimated to be 85%, which is larger than the 75% reported in Bramson et al. (2015) using the Eq. (1) with $\gamma = 2.7$, and the zero-porosity values of ϵ' of water ice and dust used by Bramson et al. (2015), i.e., 3.15 and 8, respectively.

Table 4 also lists the parameters of Eq. (5) for the center-band frequencies of MARSIS and for the lower and upper limits of the frequency range of the WISDOM radar using the same method. The MARSIS signal penetrates deeper than that of SHARAD, and thus is able to detect materials at depth that may have different compositions. Therefore, it is useful to have the ability to apply the same dielectric model – albeit tuned to the relevant frequencies – to data from both instruments in order to quantify these possible differences.

The WISDOM instrument that will be part of the ExoMars 2020 rover, will use higher frequency radar to probe the top few meters of the Martian subsurface with a resolution of up to 3 cm (Ciarletti et al., 2017). The frequency range of our microwave instrument encompasses the operational range of the WISDOM radar, so in principle, our measurements are directly relevant to the interpretation of WISDOM data.

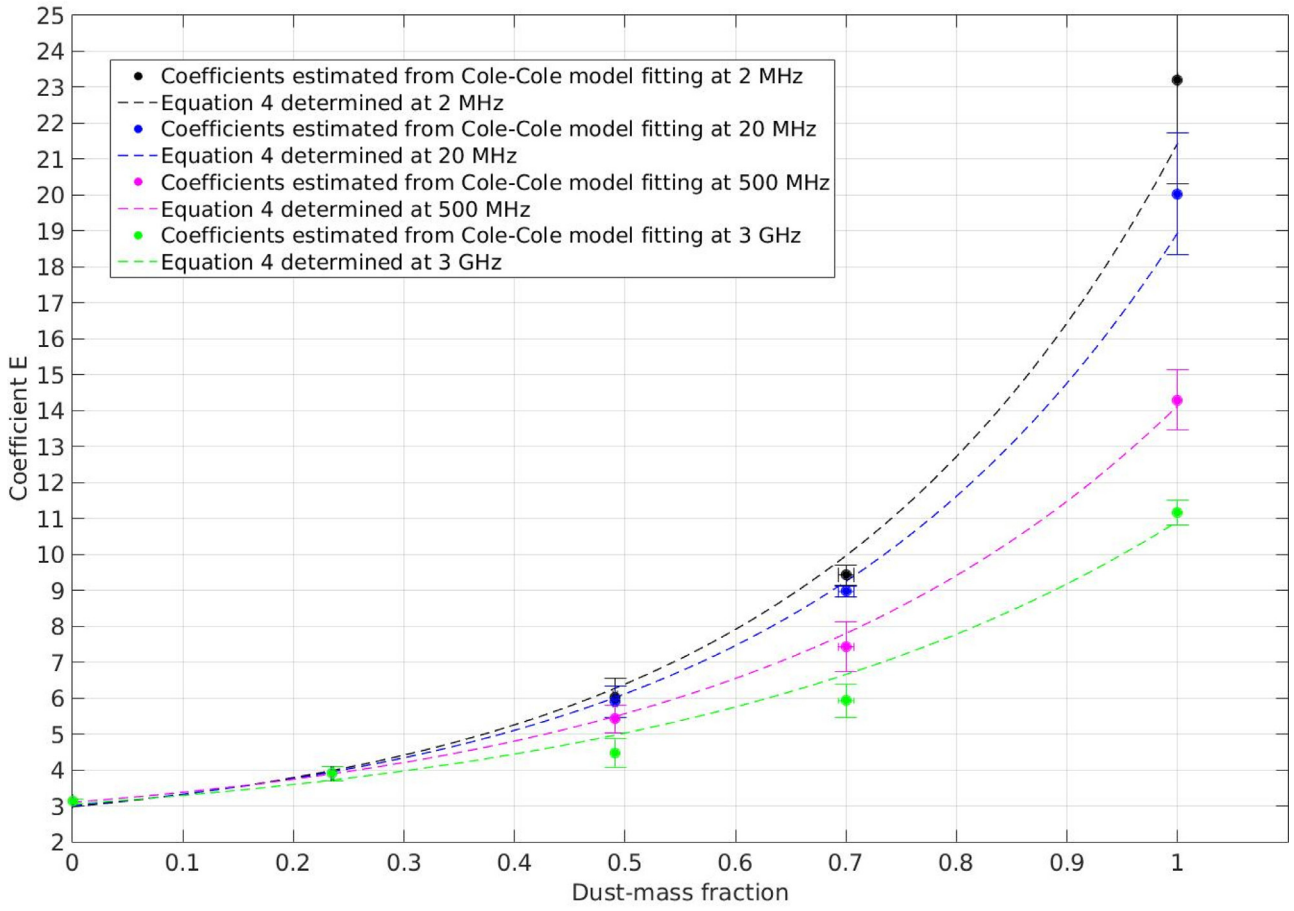

Fig. 8. E coefficients obtained from Eq. (4) as a function of the dust mass fraction of the sample. At a given frequency, E increases with dust mass fraction. For $F_D = 1$, results for samples #5–9 are taken into account; for $F_D = 0.70$, samples #10–14; for $F_D = 0.49$, samples #15–18; for $F_D = 0.24$, samples #19–23. For $F_D = 0$, results for samples #1–13 reported in Brouet et al. (2016) are used. The power-law used in the fit is given by Eq. (4) in the main text. For each case, the correlation coefficient is larger than 0.98 and the fit coefficients of the power-law are estimated with 95% confidence.

Table 4
Values of the free parameters P_1 and P_2 retrieved with Eq. (4).

Radar	Frequency (MHz)	P_1	P_2
MARSIS	2	19.46 ± 1.26	1.98 ± 0.21
SHARAD	20	16.94 ± 0.75	2.00 ± 0.16
WISDOM	500	12.03 ± 0.27	2.10 ± 0.06
	3000	8.87 ± 0.53	2.05 ± 0.19

The ExoMars 2020 rover landing site candidates have been down-selected to two locations: Oxia Planum (18.20°N, 335.45°E) located to the East of the Chryse Planitia lowlands, and Mawrth Vallis (22°N, 342°E), a large outflow channel located at the margin between Arabia Terra and Chryse Planitia. The importance of these locations lies in the abundance of phyllosilicates (clay minerals produced by chemical weathering) detected here. These deposits provide a window into the history of aqueous activity on early Mars and allow the investigation of possible habitable environments that may have existed during the Noachian period (~ 4.5 to ~ 3.6 Ga). However, it is unlikely that locations in such low latitudes will contain stable subsurface excess ice at such shallow depths (Mellon et al., 2004), for which the results of this paper could be directly applicable. Aside from the remotely detected clay deposits at the surface, there is nevertheless some uncertainty regarding what a sub-surface probe such as WISDOM would find at these latitudes. A recent study by Wilson et al. (2018) improved the results of the Mars Odyssey Neutron Spectrometer to show evidence for buried ice at near-equatorial locations such as the Medusa Fossae Formation and the western slopes of the Tharsis Montes and Elysium Mons. Therefore, although unlikely based on the current data, the possibility remains that WISDOM could observe permittivity interfaces in the shallow subsurface that may be consistent with water ice and dust mixtures. In addition, the method described in this paper can be directly applied without many modifications to investigate the electrical properties of terrestrial clays and other simulants that may be more directly relevant to the ExoMars 2020 rover landing site, given the current state of knowledge on the geochemistry of these sites.

Finally, it is important to again note that our method and resulting dielectric mixing model are based on the assumption that the targeted material is nonmagnetic and has low dielectric loss. We must emphasize that neglecting dielectric losses may lead to an overestimation of the upper limit of the water ice volume fraction, as shown by Campbell and Morgan (2018) for Arcadia (Bramson et al., 2015) and Utopia (Stuurman et al., 2016) Planitiae. In their paper, Campbell and Morgan (2018) propose a new method to estimate the loss tangent (ϵ''/ϵ') based on splitting the 10 MHz bandwidth of the SHARAD signal into lower resolution radargrams corresponding to three sub-bands, and determining the variation in attenuation as a function of the free-space wavelength. This method leads to reasonable estimates of the loss tangent for sedimentary, volcanic, and mantling deposits for non-polar materials, and allows a first-order discrimination of ice-rich from ice-poor materials.

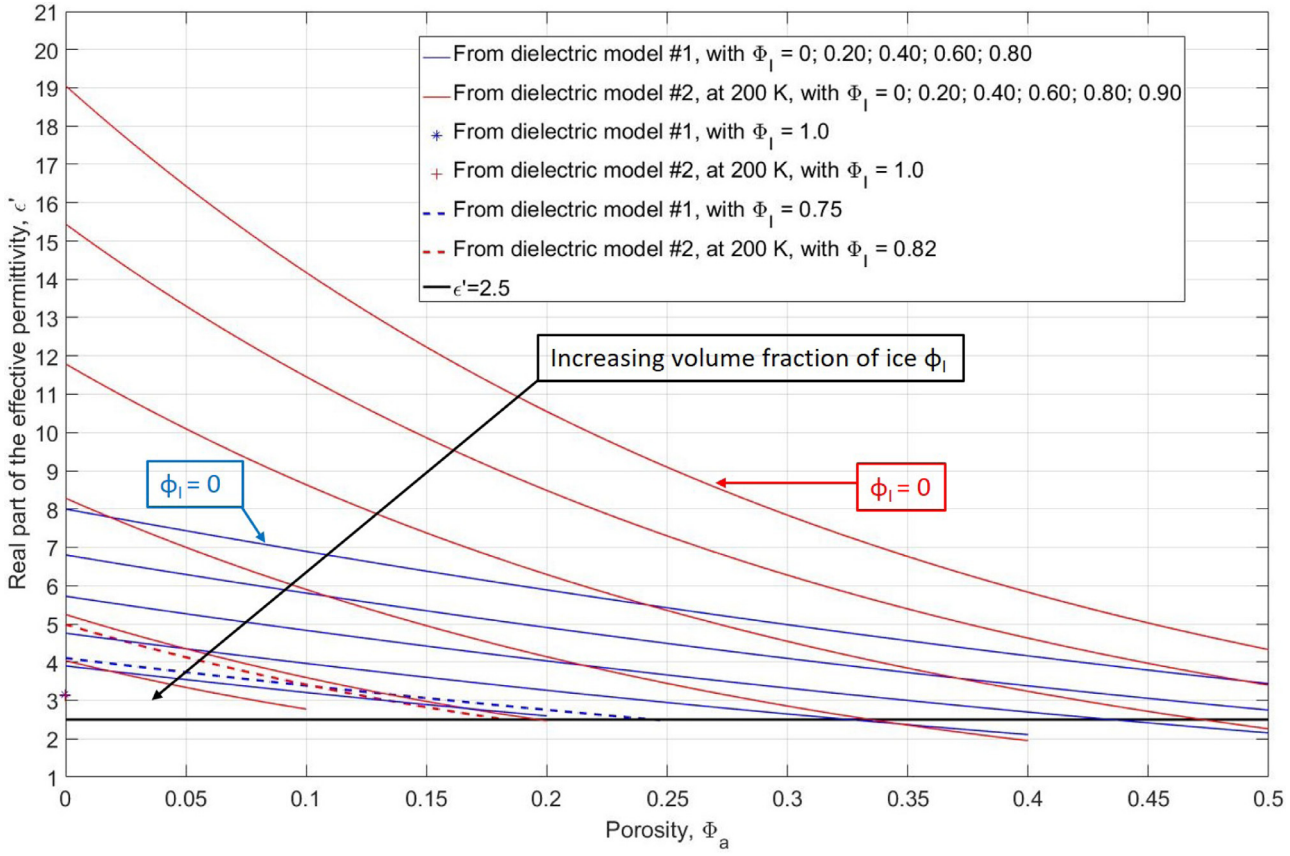

Fig. 9. Comparison of the porosity (Φ_a) dependence of the real part of the permittivity (ϵ') calculated from dielectric models #1 and #2 for different values of water ice volume fraction (Φ_I). Model #1 is based on Eq. (1), with $\gamma = 2.7$, and with the zero-porosity values of ϵ' for water ice and dust used by Bramson et al. (2015), i.e., 3.15 and 8, respectively. Model #2 is based on Eq. (5), with parameters estimated for a frequency of 20 MHz and assuming a Martian mean surface temperature of 200 K. The horizontal black line represents a value of ϵ' derived from SHARAD radargrams (Bramson et al., 2015). The dashed blue curve (ϵ' vs. porosity for $\Phi_I = 0.75$ obtained from Model #1) intersects the horizontal black line, while the solid blue curve (Model #1, $\Phi_I = 0.80$) does not, meaning that the upper limit of Φ_I is ~ 0.75. The dashed red curve, (ϵ' vs. porosity for $\Phi_I = 0.82$ obtained from Model #2, with $P_2 = 2.16$), intersects the horizontal black line, while the solid red curve (Model #2, $\Phi_I = 0.90$) does not, meaning that the upper limit of Φ_I is ~ 0.82. (For interpretation of the references to colour in this figure legend, the reader is referred to the web version of this article.)

5. Summary and conclusions

We measured the dielectric properties of JSC Mars-1 at ambient temperature and at 243 K, and of mixtures of water ice and JSC Mars-1 at 243 K, in the radar frequencies between 50 MHz and 2 GHz. For different ice mass fractions, we determined the porosity dependence of the real part of the permittivity, using a sample preparation method and a data acquisition method previously validated for similar studies in the same frequency range (Brouet et al., 2016). The porosity values covered by the measurements at 300 K and 243 K for pure JSC Mars-1 samples are in the range of 64% to 71%. For the mixtures, this range is between 40% and 60%. The porosity dependence of ϵ' for pure water ice is well constrained for porosities between 0 and 86% (Brouet et al., 2016). Considering these ranges in porosity and the unique constraint imposed by the model proposed here (i.e., for a porosity equal to 1 then $\epsilon' = 1$), the extrapolation of this model toward low values of porosity should provide reliable results (within the uncertainties) when used for the inversion of radar data. We derived dielectric models valid at the operating frequencies of the SHARAD and MARSIS radar sounders, as well as at the lower and upper limits of the operating frequency range of the WISDOM ground penetrating radar. These models relate the real part of the permittivity to the volume fractions of pure water ice and JSC Mars-1, the porosity and the temperature. For a given dielectric constant, our model at SHARAD centre-band frequency infers a larger volume fraction of water ice than that found by prior studies that interpreted SHARAD radargrams of the mid-latitudes of Mars using the model of Stillman et al. (2010), for which a sand sample with high-purity silica was used as a Martian dust analogue and the porosity dependence of the dielectric constant was based on a theoretical dielectric mixing law.

Dielectric mixing models like that of Stillman et al. (2010) and the one presented here are determined from measurements of mixtures of specific components (e.g., water ice or saline water ice, air, and sand or JSC Mars-1). We argue that our model is more directly relevant to certain Martian surface and subsurface compositions, however these models should in general be applied with caution to interpret the dielectric properties of materials with probable compositions that do not include a mixture of these components.

Finally, in order to accurately interpret data collected by radar exploration of the Martian subsurface at non-polar areas (such as that planned for WISDOM) we suggest that the application of the model described in this paper be systematically combined with the split-chirp radargram analysis method of Campbell and Morgan (2018). The combination of these complementary techniques can avoid the inference of unrealistic geologic and climatic scenarios developed from a biased interpretation of the electromagnetic properties of the subsurface materials.

Acknowledgments

Support from the Swiss National Science Foundation is acknowledged (grant number: 200020_178847). Data used for this study can be accessed through direct communication with the corresponding author

(Yann Brouet; e-mail: yann.brouet@space.unibe.ch).

References

Allen, C.C., Jager, K.M., Morris, R.V., et al., 1998. Martian soil simulant available for scientific, educational study. EOS Trans. Am. Geophys. Union 79, 405–409. https://doi.org/10.1029/98EO00309.

Audouard, J., Poulet, F., Vincendon, M., et al., 2014. Water in the Martian regolith from OMEGA/Mars Express. J. Geophys. Res. 119, 1969–1989. https://doi.org/10.1002/2014JE004649.

Bartels-Rausch, T., Bergeron, V., Cartwright, J.H.E., et al., 2012. Ice structures, patterns, and processes: a view across the ice fields. Rev. of Mod. Phys. 84, 885–944. https://doi.org/10.1103/RevModPhys.84.885.

Bramson, A.M., Byrne, S., Bapst, J., 2017. Preservation of midlatitude ice sheets on Mars. J. Geophys. Res. 122, 2250–2266. https://doi.org/10.1002/2017JE005357.

Bramson, A.M., Byrne, S., Putzig, N., et al., 2015. Widespread excess ice in Arcadia Planitia, Mars. Geophys. Res. Lett. 42, 6566–6574. https://doi.org/10.1002/2015GL064844.

Brouet, Y., Neves, L., Sabouroux, P., et al., 2016. Characterization of the permittivity of controlled porous water ice-dust mixtures to support the radar exploration of icy bodies. J. Geophys. Res. Planets 121 (12), 2426–2443. https://doi.org/10.1002/2016JE005045.

Byrne, S., 2009. The Polar deposits of Mars. Annu Rev Earth Planet Sci. 37 (1), 535–560. https://doi.org/10.1146/annurev.earth.031208.100101.

Calla, O., Rathore, I., 2012. Study of complex dielectric properties of lunar simulants and comparison with Apollo samples at microwave frequencies. Adv. Space Res. 50, 1607–1614. https://doi.org/10.1016/j.asr.2012.07.031.

Campbell, B., Morgan, G., 2018. Fine-scale layering of Mars Polar deposits and signatures of ice content in non-polar material from multi-band SHARAD data processing. Geophys. Res. Lett. 45, 1759–1766. https://doi.org/10.1002/2017GL075844.

Campbell, M., Ulrichs, J., 1969. Electrical properties of rocks and their significance for lunar radar observations. J. Geophys. Res. 74, 5867–5881. https://doi.org/10.1029/JB074i025p05867.

Ciarletti, V., Clifford, S., Plettemeier, D., et al., 2017. The WISDOM radar: unveiling the subsurface beneath the ExoMars rover and identifying the best locations for drilling. Astrobiology 17, 565–584. https://doi.org/10.1089/ast.2016.1532.

Cole, K., Cole, R., 1941. Dispersion and absorption in dielectrics. J. Chem. Phys. 9, 341–351. https://doi.org/10.1063/1.1750906.

Debye, P., 1929. Polar molecules. J. Soc. Chem. Ind. 48, 1036–1037. https://doi.org/10.1002/jctb.5000484320.

Dundas, C., Bramson, A., Ojha, L., et al., 2018. Exposed subsurface ice sheets in the Martian mid-latitudes. Science 359, 199–201. https://doi.org/10.1126/science.aao1619.

Georget, E., Abdeddaim, R., Sabouroux, P., 2014. A quasi-universal method to measure the electromagnetic characteristics of usual materials in the microwave range. C. R. Phys. 15, 448–457. https://doi.org/10.1016/j.crhy.2014.02.003.

Gough, S.R., 1972. A low temperature dielectric cell and the permittivity of hexagonal ice to 2K. Can. J. Chem. 50, 3046–3051. https://doi.org/10.1139/v72-483.

Heggy, E., Paillou, P., Ruffie, G., et al., 2001. On water detection in the Martian subsurface using sounding radar. Icarus 154, 244–257. https://doi.org/10.1006/icar.2001.6717.

Heldmann, J., Schurmeier, L., McKay, C., Davila, A., Stoker, C., Marinova, M., Wilhelm, M., 2014. Midlatitude Ice-rich ground on Mars as a target in the search for evidence of life and for in situ resource utilization on human missions. Astrobiology 14, 102–118. https://doi.org/10.1089/ast.2013.1103.

Holt, J.W., Peters, M., Kempf, S., Morse, D., Blankenship, D., 2006. Echo source discrimination in single-pass airborne radar sounding data from the Dry Valleys, Antarctica: implications for orbital sounding of Mars. J. Geophys. Res. 111 (E06S24). https://doi.org/10.1029/2005JE002525.

Jordan, R., Picardi, G., Plaut, J., et al., 2009. The Mars express MARSIS sounder instrument. Planet. Space Sci. 57, 1975–1986. https://doi.org/10.1016/j.pss.2009.09.016.

Laskar, J., Correia, A., Gastineau, M., Joutel, F., 2004. Long term evolution and chaotic diffusion of the insolation quantities of Mars. Icarus 170, 343–364. https://doi.org/10.1016/j.icarus.2004.04.005.

Leuschen, C., 1999. Analysis of the complex permittivity and permeability of a Martian soil simulant from 10 MHz to 1 GHz, Proceedings IEEE Geoscience and Remote Sensing Symposium 4, 264–266. doi:10.1109/IGARSS.1999.775096.

Lide, A., 2005. Handbook of Chemistry and Physics. CRC Press, Florida.

Looyenga, H., 1965. Dielectric constants of heterogeneous mixtures. Physica 31, 401–406. https://doi.org/10.1016/0031-8914(65)90045-5.

Mattei, E., Lauro, S.E., Vannaroni, G., et al., 2014. Dielectric measurements and radar attenuation estimation of ice/basalt sand mixtures as Martian Polar Caps analogues. Icarus 229, 428–433. https://doi.org/10.1016/j.icarus.2013.10.017.

Mätzler, C., Wegmuller, U., 1987. Dielectric properties of freshwater ice at microwave frequencies. J. Phys. D App. Phys. 20, 1623–1630. https://doi.org/10.1088/0022-3727/20/12/013.

Mellon, M., Feldman, W., Prettyman, T., 2004. The presence and stability of ground ice in the southern hemisphere of Mars. Icarus 169, 324–340. https://doi.org/10.1016/j.icarus.2003.10.022.

Nerozzi, S., Holt, J. W., 2018. Ice caps under sand caps under an ice cap: revealing a record of climate change on Mars with SHARAD, Proceedings of the 49th Lunar and Planetary Science Conference LPI Contrib. No. 2083.

Nicolson, A.M., Ross, G., 1970. Measurement of the intrinsic properties of materials by time-domain techniques. IEEE Trans. Instr. Meas. 19, 377–382. https://doi.org/10.1109/TIM.1970.4313932.

Ojha, L., Lewis, K., 2018. The density of the Medusae Fossae Formation: Implications for its composition, origin, and importance in Martian history. J. Geophys. Res. Planets 123, in press. https://doi.org/10.1029/2018JE005565.

Olhoeft, G.R., Strangway, D.W., 1975. Dielectric properties of the first 100 meters of the moon. Earth Planet. Sc. Lett. 24, 394–404. https://doi.org/10.1016/0012-821X(75)90146-6.

Pettinelli, E., Vannaroni, G., Cereti, A., et al., 2005. Laboratory investigations into the electromagnetic properties of magnetite/silica mixtures as Martian soil simulants. J. Geophys. Res. 110 (E04013). https://doi.org/10.1029/2004JE002375.

Poch, O., Pommerol, A., Jost, B., et al., 2016. Sublimation of water ice mixed with silicates and tholins: evolution of surface texture and reflectance spectra. Icarus 267, 154–173. https://doi.org/10.1016/j.icarus.2015.12.017.

Sabouroux, P., Ba, D., 2011. EPSIMU, a tool for dielectric properties measurement of porous media: application in wet granular materials characterization. Pr. Electromagn. Res. 29, 191–207. https://doi.org/10.2528/PIERB10112209.

Schmidt, R., 2003. Mars Express-ESA's first mission to planet Mars. Acta Astronaut. 52, 197–202. https://doi.org/10.1016/S0094-5765(02)00157-1.

Seu, R., Biccari, D., Orosei, R., et al., 2004. SHARAD: the MRO 2005 shallow radar. Planet. Space Sci. 52, 157–166. https://doi.org/10.1016/j.pss.2003.08.024.

Sihvola, A.H., 1999. Electromagnetic Mixing Formulas and Applications. The Institution of Electrical Engineers, London, United Kingdom.

Stillman, D., Grimm, R., Dec, S., 2010. Low-frequency electrical properties of ice-silicate mixtures. J. Phys. Chem. B 114, 6065–6073. https://doi.org/10.1021/jp9070778.

Stillman, D.E., Olhoeft, G., 2008. Frequency and temperature dependence in electromagnetic properties of Martian analog minerals. J. Geophys. Res. 113 (E09005). https://doi.org/10.1029/2007JE002977.

Stuurman, C., Osinski, G., Holt, J.W., et al., 2016. SHARAD detection and characterization of subsurface water ice deposits in Utopia Planitia, Mars. Geophys. Res. Lett. 43, 9484–9491. https://doi.org/10.1021/jp9070778.

Ulaby, F.T., Long, D.G., 2014. Microwave Radar and Radiometric Remote Sensing. University of Michigan Press, Ann Arbor, Michigan.

Williams, K., Greeley, R., 2004. Measurements of dielectic loss factors due to a Martian dust analog. J. Geophys. Res. 109 (E10006). https://doi.org/10.1029/2002JE001957.

Wilson, J., Eke, V., Massey, R., et al., 2018. Equatorial locations of water on Mars: improved resolution maps based on Mars Odyssey Neutron Spectrometer data. Icarus 299, 148–160. https://doi.org/10.1016/j.icarus.2017.07.028.

Yoldi, Z., Pommerol, A., Jost, B., et al., 2015. VIS-NIR reflectance of water ice/regolith analogue mixtures and implications for the detectability of ice mixed within planetary regoliths. Geophys. Res. Lett. 42 (15), 6205–6212. https://doi.org/10.1002/2015GL064780.

Zurek, R.W., Smrekar, S.E., 2007. An overview of the Mars Reconnaissance Orbiter (MRO) science mission. J. Geophys. Res. 112 (E05S01). https://doi.org/10.1029/2006JE002701.